Collision rate coefficient for charged dust grains in the presence of linear shear

Huan Yang and Christopher J. Hogan, Jr.*

Department of Mechanical Engineering, University of Minnesota, 111 Church Street S.E., Minneapolis, Minnesota 55455, USA

(Received 17 May 2017; revised manuscript received 10 July 2017; published 18 September 2017)

Like and oppositely charged particles or dust grains in linear shear flows are often driven to collide with one another by fluid and/or electrostatic forces, which can strongly influence particle-size distribution evolution. In gaseous media, collisions in shear are further complicated because particle inertia can influence differential motion. Expressions for the collision rate coefficient have not been developed previously which simultaneously account for the influences of linear shear, particle inertia, and electrostatic interactions. Here, we determine the collision rate coefficient accounting for the aforementioned effects by determining the collision area, i.e., the area of the plane perpendicular to the shear flow defining the relative initial locations of particles which will collide with one another. Integration of the particle flux over this area yields the collision rate. Collision rate calculations are parametrized as an enhancement factor, i.e., the ratio of the collision rate considering potential interactions and inertia to the traditional collision rate considering laminar shear only. For particles of constant surface charge density, the enhancement factor is found dependent only on the Stokes number (quantifying particle inertia), the electrostatic energy to shear energy ratio, and the ratio of colliding particle radii. Enhancement factors are determined for Stokes numbers in the 0–10 range and energy ratios up to 5. Calculations show that the influences of both electrostatic interactions and inertia are significant; for inertialess (St = 0) equal-sized and oppositely charged particles, we find that even at energy ratios as low as 0.2, enhancement factors are in excess of 2. For the same situation but like-charged particles, enhancement factors fall below 0.5. Increasing the Stokes number acts to mitigate the influence of electrostatic potentials for both like and oppositely charged particles; i.e., inertia reduces the enhancement factor for oppositely charged particles and increases it for like-charged particles. Uniquely, at elevated Stokes numbers with attractive potentials we find collisionless "pockets" within the collision area, which are regions completely bounded by the collision area but within which collisions do not occur. Regression equations to results are provided, enabling calculation of the enhancement factor as a function of energy ratio and Stokes number. In total, this study both leads to insight into the collision dynamics of finite-inertia, charged particles in shear flows, and provides a means to simply calculate the particle-particle collision rate coefficient.

DOI: 10.1103/PhysRevE.96.032911

I. INTRODUCTION

Collisions between micrometer-sized charged particles or dust grains have a large influence on the behavior of many colloidal [1], aerosol [2,3], granular [4–6], and dusty plasma [7–9] systems. For example, in fluidized beds, dust storms, and volcanic plumes, particle-particle collisions lead to charge exchange (even for identical chemical composition particles [4,10–12]), which can significantly alter the behavior of a particle-laden flow [13–15]. In aerosols and dusty plasmas, oppositely charged particles rapidly aggregate (collide and bind) with one another, while the charging of particles to sufficiently high levels of the same polarity stabilizes them against aggregation [16–20]. Given the importance of charged particle collisions in particle-laden flows, numerous efforts have been devoted to developing accurate collision rate models for charged particles [21–23]. Many of these efforts consider the combined influences of electrostatic potential interactions and thermal energy on particle motion, such that the number of collisions per unit volume per unit time (R_{ij}) between particles of type i (size, charge level) and type j can be calculated as

$$R_{ij} = k_{ij} n_i n_j, \tag{1}$$

where n_i and n_j are the number concentrations of particles of type i and type j, respectively, and k_{ij} is the collision rate coefficient. In particular, in liquid colloids, the approach of Fuchs [24] has been used to calculate collision rate coefficients considering Brownian motion (continuum regime thermal motion) and combined electrostatic and van der Waals potential interactions (i.e., DLVO interactions) [25]. In reduced pressure systems, the effects of thermal energy and electrostatic forces have been incorporated into orbital motion limited (OML) theory based collision rate coefficient predictions [26–28]. A variety of approaches have also been utilized to derive collision rate expressions between the colloidal (diffusive) and low-pressure (ballistic) limits [29–33], both for particles with one another as well as particles with ions. In large part, the aforementioned collision rate expressions have shown good agreement with experimental measurements [34,35]; thus their incorporation into population balance models of particle ensembles is commonplace [36].

However, for micrometer-sized particles in flowing systems, the influence of thermal energy on particle motion is often negligible in comparison to the influence that laminar (linear) shear gradients have on particle differential motion. This differential motion can lead to an enhanced rate of collisions (so-called orthokinetic aggregation) between particles as compared to consideration of thermal energy alone [37]. In the absence of any electrostatic interactions, the collision rate coefficient for spherical particles of radii a_i and a_j in the presence of a linear shear gradient G was first derived by Smoluchowski [38], and is given as

$$k_{ij} = \tfrac{4}{3} G (a_i + a_j)^3. \tag{2a}$$

*Corresponding author: hogan108@.umn.edu

A number of studies have examined the combined influence of DLVO-like potential interactions (wherein particles electrostatically repel one another but attract one another at close approach via van der Waals interactions) and laminar shear gradients on particle collisions; collision rate coefficients derived considering these two approaches apply specifically to particles in liquid colloids [39–41]. However, a collision rate expression considering the combined influences of laminar shear and electrostatic potential interactions (both attractive and repulsive), which can be applied to particles in gaseous media (including granular systems, aerosols, clouds, and dust storms) remains undeveloped, despite the fact that in many gas phase systems, both electrostatic interactions and shear play a role in governing particle-particle collisions. The specific issues which remain to be addressed in modeling collisions in such systems are twofold. First, when following the derivation of Eq. (2a) but considering attractive electrostatic interactions, the collision area (defined subsequently) approaches infinity. This complicates calculation of the integral required to determine the collision rate coefficient. Second, unlike liquid colloidal suspensions, larger shear gradients can persist in gaseous systems, and as such the influence of particle inertia on motion in a combined electrostatic and shear field can be significant. Prior approaches to collision rate coefficient evaluation have neglected particle inertial influences.

The purpose of this work is to utilize a trajectory based calculation approach to find an expression for the particle-particle collision rate coefficient in the presence of a linear shear gradient and electrostatic potential interactions, while also accounting for finite particle inertia. The resulting calculations are parametrized as an enhancement factor, η_L, such that the collision rate coefficient can be calculated in a manner analogous to Eq. (2a):

$$k_{ij} = \tfrac{4}{3} G (a_i + a_j)^3 \eta_L. \tag{2b}$$

The sections that follow provide details on the trajectory calculations employed as well as on incorporation of trajectory calculation results into enhancement factor calculations. Subsequently, calculation results are presented considering simple Coulomb potentials as well as fully resolved electrostatic interactions for conducting particles. We parametrize enhancement factors as functions of a dimensionless electrostatic to shear energy ratio, the Stokes number, and the particle-size (radius) ratio. The resulting expressions are applicable for calculations of particle-particle collision rates in gases wherein both shear gradients and electrostatic effects influence particle motion, but with thermal motion negligible.

II. THEORETICAL AND NUMERICAL APPROACH

In Sec. II A we derive the nondimensionalized equation of motion applicable to particles used in collision rate determination (considering simple Coulomb and full electrostatic potential interactions), and then in Sec. II B we discuss the numerical methods employed to carry out trajectory and enhancement factor calculations. Readers not concerned with the details of calculations can directly focus on the Results and Discussion section without significant loss of scope.

A. Motion of charged particle pairs in a laminar shear field

Collisions can be modeled by examining particle pairs (i.e., we consider one particle i and a second j). The equation of motion for each charged particle in a linear shear field of magnitude G is given by

$$m \frac{d^2 \vec{R}(t)}{dt^2} = f \left\{ \vec{u}[\vec{R}(t)] - \frac{d\vec{R}(t)}{dt} \right\} + \vec{F}_e, \tag{3}$$

where m is the particle mass, $\vec{R}$ its position, $\vec{u}$ is the fluid velocity field (i.e., $\vec{u}(x,y,z) = -Gy\hat{e}_z$, where $\hat{e}_z$ is the unit vector in the z direction and x, y, z are coordinates of an arbitrary point in a linear shear field with a gradient in the y direction), and $\vec{F}_e$ is the electrostatic force between particles. In writing Eq. (3), Stokes drag is assumed, hence the drag coefficient takes the form of $f = 6\pi\mu a$, where a is the particle radius and μ is the gas dynamic viscosity. We find this is a reasonable assumption for the particle velocities obtained in trajectory simulations here, even in situations where the Stokes number is high. We note, however, that we have neglected the slip correction factor [42] in our drag formulation. The slip correction factor could be easily incorporated into the subsequently presented dimensionless ratios with minimal modification to results. We also neglect the influences of viscous interactions [43] between particles at close approach, as well as Saffman lift forces [44]. We anticipate both influences are small for submicrometer to supermicrometer particles in the gas phase.

The electrostatic force acting on each particle can be obtained by differentiating the induced electrostatic potential energy, W:

$$\vec{F}_e = -\frac{dW}{dr_{ij}} \hat{r}, \tag{4}$$

where $\hat{r}$ is the unit vector pointing from the center of the opposite particle to the present particle and r_{ij} is the scalar distance between particle centers. We examine interactions between nonconducting and perfectly conducting particles in the dilute limit. Under these conditions, the influence of screening on potentials is negligible (i.e., there is an infinite screening length). At the same time, when particles are far from one another, though potential interactions between particles are not screened, the effects of electrostatic forces on particle motion are negligible when compared to the effects of shear. Further, multibody interactions need not be considered in the dilute limit, as the probability that a third particle is in the vicinity of two particles closely approaching one another is zero. For nonconducting particles which have not yet collided, a simple two-body Coulomb potential is hence assumed, such that the potential energy between them can be expressed as

$$W = \frac{q_i q_j}{4\pi\varepsilon_0 r_{ij}}, \tag{5}$$

where q is the charge carried by each of the particles and ε_0 is the vacuum permittivity. For perfectly conducting particles, we utilize the functional form [45]:

$$W = \frac{q_i^2 c_{jj} - 2q_i q_j c_{ij} + q_j^2 c_{ii}}{8\pi\varepsilon_0 \left(c_{ii} c_{jj} - c_{ij}^2\right)}, \tag{6a}$$

where c_{ii}, c_{jj}, and c_{ij} are the coefficients of capacitance, which are expressed as [46]

$$c_{ii} = a_i(1-\kappa^2)\sum_{m=0}^{\infty}\frac{\alpha^m}{1-\kappa^2\alpha^{2m}}, \tag{6b}$$

$$c_{ij} = -\frac{a_i a_j}{r_{ij}}(1-\alpha^2)\sum_{m=0}^{\infty}\frac{\alpha^m}{1-\alpha^{2(1+m)}}. \tag{6c}$$

The dimensionless parameters α and κ are given by

$$\alpha = \frac{r_{ij}^2 - a_i^2 - a_j^2}{2a_i a_j} - \sqrt{\left(\frac{r_{ij}^2 - a_i^2 - a_j^2}{2a_i a_j}\right)^2 - 1}, \tag{6d}$$

$$\kappa = \frac{a_i + \alpha a_j}{r_{ij}}. \tag{6e}$$

c_{jj} can be obtained by replacing a_i with a_j, and vice versa in the expression of c_{ii}.

We define $t^* = Gt$, $\vec{R}^* = \vec{R}/(a_i + a_j)$, $\vec{u}^* = -y^*\hat{e}_z$ (where y^* is the y coordinate also normalized by $a_i + a_j$), $W^* = 4\pi\varepsilon_0(a_i + a_j)W/q_i q_j$, $r_{ij}^* = r_{ij}/(a_i + a_j)$, and $c^* = c/(a_i + a_j)$. The dimensionless equations of motion for particles i and j can then be obtained by combining Eqs. (3)–(5) (for nonconducting particles), or Eqs. (3) and (6a)–(6c) (for conducting particles). For nonconducting particles the dimensionless equations are

$$\frac{d^2\vec{R}_i^*}{dt^{*2}} = (1-\theta_m)\frac{Q}{St}\frac{\vec{R}_j^* - \vec{R}_i^*}{r_{ij}^{*3}} - \frac{1-\theta_m}{(1-\theta_f)St} \times\left[\frac{d\vec{R}_i^*}{dt^*} - \vec{u}^*(\vec{R}_i^*)\right], \tag{7a}$$

$$\frac{d^2\vec{R}_j^*}{dt^{*2}} = \theta_m\frac{Q}{St}\frac{\vec{R}_i^* - \vec{R}_j^*}{r_{ij}^{*3}} - \frac{\theta_m}{\theta_f St}\left[\frac{d\vec{R}_j^*}{dt^*} - \vec{u}^*(\vec{R}_j^*)\right]. \tag{7b}$$

For conducting particles the dimensionless equations are

$$\frac{d^2\vec{R}_i^*}{dt^{*2}} = (1-\theta_m)\frac{Q}{St}\frac{\vec{R}_i^* - \vec{R}_j^*}{r_{ij}^*}\frac{dW^*}{dr_{ij}^*} - \frac{1-\theta_m}{(1-\theta_f)St} \times\left[\frac{d\vec{R}_i^*}{dt^*} - \vec{u}^*(\vec{R}_i^*)\right], \tag{8a}$$

$$\frac{d^2\vec{R}_j^*}{dt^{*2}} = \theta_m\frac{Q}{St}\frac{\vec{R}_j^* - \vec{R}_i^*}{r_{ij}^*}\frac{dW^*}{dr_{ij}^*} - \frac{\theta_m}{\theta_f St}\left[\frac{d\vec{R}_j^*}{dt^*} - \vec{u}^*(\vec{R}_j^*)\right]. \tag{8b}$$

$\frac{dW^*}{dr_{ij}^*}$ can be evaluated through the dimensionless form of Eqs. (6a)–(6c):

$$W^* = \frac{\theta_q c_{jj}^* - 2c_{ij}^* + 1/\theta_q c_{ii}^*}{2\left(c_{jj}^* c_{ii}^* - c_{ij}^2\right)}, \tag{9a}$$

$$c_{ii}^* = \theta_r(1-\kappa^2)\sum_{m=0}^{\infty}\frac{\alpha^m}{1-\kappa^2\alpha^{2m}}, \tag{9b}$$

$$c_{ij}^* = -\frac{\theta_r(1-\theta_r)}{r_{ij}^*}(1-\alpha^2)\sum_{m=0}^{\infty}\frac{\alpha^m}{1-\alpha^{2(1+m)}}, \tag{9c}$$

with the definitions $\alpha = \frac{r_{ij}^{*2}-1+2\theta_r(1-\theta_r)}{2\theta_r(1-\theta_r)} - \sqrt{\left[\frac{r_{ij}^{*2}-1+2\theta_r(1-\theta_r)}{2\theta_r(1-\theta_r)}\right]^2 - 1}$, $\kappa = \frac{\theta_r+\alpha(1-\theta_r)}{r_{ij}^*}$, $\theta_q = \frac{q_i}{q_j}$, and $\theta_r = \frac{a_i}{a_i+a_j}$. In calculating dimensionless potentials with Eqs. (9b) and (9c) the number of terms retained in series (m_t) is determined by calculating the value of the series $\sum_{m=m_t+1}^{\infty}(\frac{\alpha^m}{1-\kappa^2})$ and the series $\sum_{m=m_t+1}^{\infty}(\frac{\alpha^m}{1-\alpha^2})$, for Eqs. (9b) and (9c), respectively. These series have sums which are straightforward to calculate and are the respective upper limits for the series terms in (9b) and (9c). m_t is selected such that the upper limits are smaller than 0.01.

The dimensionless equations of motion show that the system, and hence the enhancement factor, is governed by six parameters: Q, St, θ_m, θ_f, θ_r, and θ_q (though θ_q only comes into play for conducting particles). They are the ratio of potential to kinetic energy, Stokes number, particle mass ratio, drag coefficient ratio, size ratio, and charge ratio, respectively. Q, St, θ_m, and θ_f are calculated with the equations:

$$Q = \frac{-q_i q_j}{4\pi\varepsilon_0 f_{ij} G(a_i + a_j)^3}, \tag{10a}$$

$$St = \frac{m_{ij} G}{f_{ij}}, \tag{10b}$$

$$\theta_m = \frac{m_i}{m_i + m_j}, \tag{10c}$$

$$\theta_f = \frac{f_i}{f_i + f_j}, \tag{10d}$$

wherein $m_{ij} = \frac{m_i m_j}{m_i+m_j}$ and $f_{ij} = \frac{f_i f_j}{f_i+f_j}$. Q takes on positive values for oppositely charged particles and negative values for like-charged particles. To reduce the number of cases necessary to examine, we note that for equivalent density particles in the continuum regime, $\theta_m = (\frac{a_i^3}{a_i^3+a_j^3}) = (\frac{\theta_r^3}{1-3\theta_r+3\theta_r^2})$ and $\theta_f = \theta_r$ [47]. Additionally, under the assumption that irrespective of polarity, particles have similar surface charge densities, $\theta_q = \frac{\theta_r^2}{-1+2\theta_r-\theta_r^2}$ for oppositely charged particles and $\theta_q = \frac{\theta_r^2}{1-2\theta_r+\theta_r^2}$ for like-charged particles. This reduces the number of cases to examine, as now the enhancement factor is a function of Q, St, and θ_r only.

B. Enhancement factor calculation

We use trajectory calculations to determine the collision rate and enhancement factor for selected Q, St, and θ_r. In calculations, initially, particle j is placed at the origin of the coordinate system, with dimensionless Cartesian coordinates x^*, y^*, and z^* (each normalized by $a_i + a_j$). Particle i is released from a surface which is perpendicular to the direction of the shear flow, and is infinitely (100 dimensionless units in simulations) far from particle j (with an initial velocity of magnitude y^*, the dimensionless y coordinate). As noted in the prior section under such conditions particle velocities are defined only by the shear field; the potential is negligible

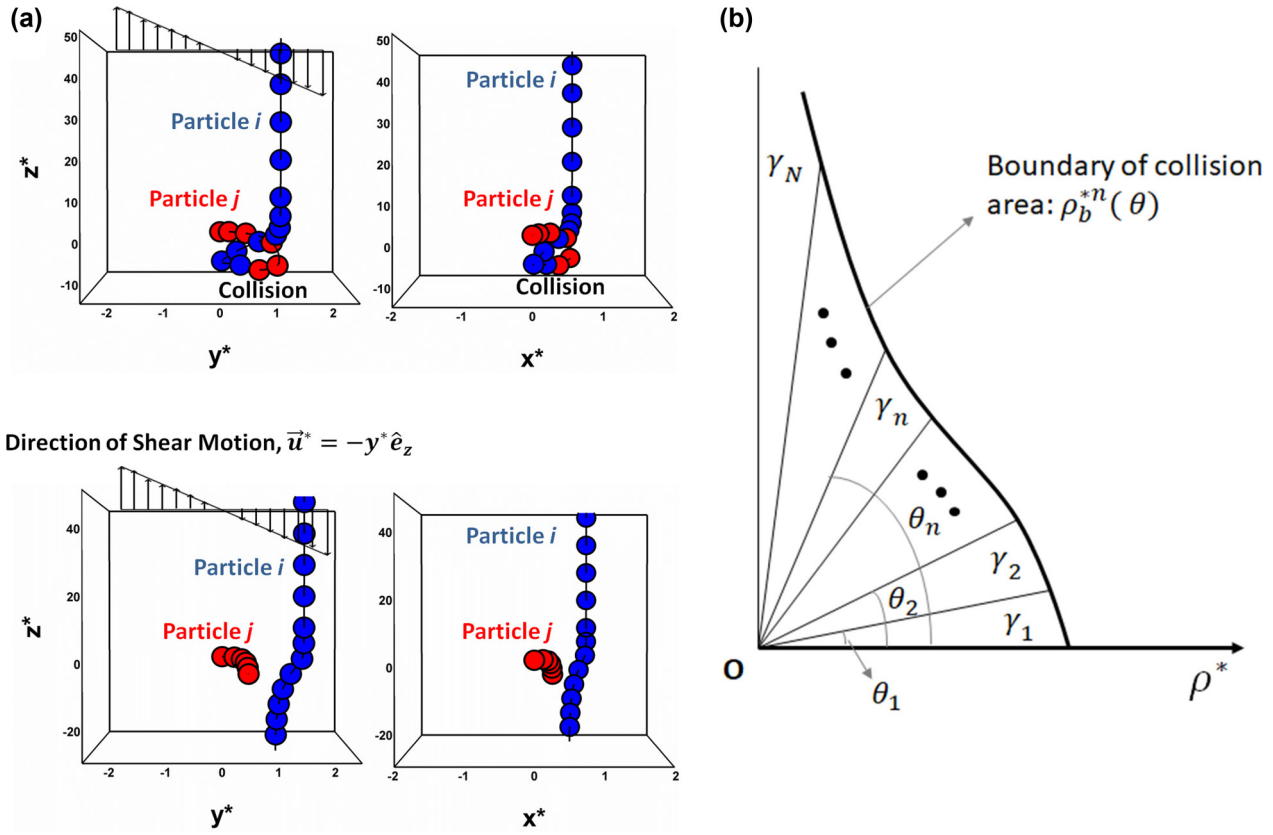

FIG. 1. (a) Example results for trajectory calculations, wherein particle j is placed in the center of a linear shear field, and particle i is placed at a specific location at a large "z^*" distance from particle j. The trajectories displayed correspond to different Q and St values, as well as different initial positions, with the upper set corresponding to a collision, and the lower corresponding to a noncollision. Particle j only moves in response to the shear field after electrostatic forces brought about by the close approach of particle i move it from its original y^* position. (b) A depiction of the dimensionless collision area formed considering attractive potentials on the y^*-x^* plane.

initially. For each condition examined the equations of motion solutions are obtained via the Euler method with a fixed maximum distance traveled by each particle during a time step (0.01 dimensionless units). A collision is considered to occur when the dimensionless center-to-center distance is less than 1.0. As demonstrated in the "Calculation validation and relative trajectories" section subsequently, we find this simple numerical algorithm is sufficient for accurate collision rate coefficient and enhancement factor determination under all circumstances. Sample trajectories are depicted in Fig. 1(a), which specifically displays two views of particle i and particle j trajectories for two different initial release positions of particle i. For both sets of trajectories, attractive potential interactions between particles are considered, but there are different Q and St values, leading to a collision (upper images, with particles partially orbiting one another prior to collision) and noncollision (lower images), respectively.

For each input Q, St, and θ_r, a dimensionless collision area (S_c^*), can be obtained by recording the initial positions of particle i which lead to collision. With this dimensionless collision area, the dimensional collision rate would be expressed as

$$k_{ij} = (a_i + a_j)^2 \iint_{S_c^*} v dS^* = (a_i + a_j)^3 G \iint_{S_c^*} y^* dS^*, \tag{11}$$

where v denotes the initial relative speed between particles, which, in the case of linear shear, is equivalent to $(a_i + a_j)Gy^*$. In the absence of potentials, particles take straight line trajectories, and collisions only occur when the particles' initial center to center distance is less than or equal to the sum of their radii. S_c^* is hence a circular area of dimensionless radius of 1.0 with its center at the origin of the polar coordinate system. Substituting $dS^* = \rho^* d\rho^* d\theta$ and $y^* = \rho^* \cos(\theta)$ into Eq. (11), where ρ^* and θ are the dimensionless polar coordinate radial position and angle, respectively, leads to Eq. (2a) in the absence of potential interactions.

Considering potentials, the dimensionless enhancement factor can then be obtained by combining Eqs. (2b) and (11):

$$\eta_L = \frac{3 \iint_{S_c^*} y^* dS^*}{4}. \tag{12}$$

We adopt slightly different approaches for enhancement factor calculations considering attractive and repulsive interactions. For attractive interactions, we utilize a polar coordinate system on the release plane for type i particles. The pole of the polar coordinate system is located at the center of the collision area, and the polar axis is parallel to the y axis. We define ρ_b^* as the dimensionless boundary of the collision area. In doing so, we assume that for $\rho^*(\theta) \leqslant \rho_b^*(\theta)$, collision can occur, and outside of it collision does not occur. Equation (12) is then

expressed as

$$\eta_{L,0} = 3\int_0^{\frac{\pi}{2}}\int_0^{\rho_b^*(\theta)} \rho^{*2}\cos(\theta)d\rho^* d\theta \quad \text{(attractive potentials)}, \tag{13}$$

where the subscript "0" denotes the "baseline" enhancement factor calculated with the aforementioned ρ_b^* assumption (collision occurs). For 30–50 specific θ values (variable for different input conditions), ρ_b^* is determined by monitoring particle trajectories releasing particle i at a dimensionless radius of 1.0 and then at successively larger radii; $\rho_b^*(\theta)$ corresponds to the largest radial location at which collision occurs. $\rho_b^*(\theta)$ is not bounded as θ approaches $\pi/2$ because the initial velocity difference between particle i and j goes to zero, and because of the long-range nature of the Coulomb potential. This complicates the calculation of the integral in Eq. (13). We hence divide the collision area into N individual areas with the angle occupied by the nth area ranging from θ_{n-1} to θ_n. The contribution to collisions for each individual area can be calculated as

$$\gamma_n = \int_{\theta_{n-1}}^{\theta_n}\int_0^{\rho_b^{*n}(\theta)} \rho^{*2}\cos(\theta)d\rho^* d\theta, \quad n = 1,2,\ldots,N-1, \tag{14}$$

$$\gamma_N = \int_{\theta_{N-1}}^{\frac{\pi}{2}}\int_0^{\rho_b^{*N}(\theta)} \rho^{*2}\cos(\theta)d\rho^* d\theta \tag{15}$$

The baseline enhancement factor is expressed as

$$\eta_{L,0} = 3\left(\sum_{n=1}^{n=N}\gamma_n\right). \tag{16a}$$

To evaluate Eqs. (14) and (15), expressions for θ_n, $\rho_b^{*n}(\theta)$, and $\rho_b^{*N}(\theta)$ need to be specified. We let $\theta_n = \frac{\pi}{2}(1-\frac{1}{8^n})$, though note that the choice of this expression is arbitrary, and adopt it simply because it rapidly approaches $\frac{\pi}{2}$ at large n. We also adopt a function of the form $\rho_b^{*n}(\theta) = A_n(\frac{1}{\frac{\pi}{2}-\theta})^{B_n} + C_n$. The coefficients A_n, B_n, and C_n are determined from the results of trajectory calculations yielding $\rho_b^{*n}(\theta)$ on the interval $\theta_{n-1} \leqslant \theta \leqslant \theta_n$. A depiction of the dimensionless collision area formed on the y^*- x^* plane, with ρ^*, θ_n, $\rho_b^{*n}(\theta)$, and γ_n each labeled, is provided in Fig. 1(b). A regression example result for determination of A_n, B_n, and C_n is provided in the Supplemental Material [48]. $\rho_b^{*N}(\theta)$ is the boundary for the collision area which consumes the angle from θ_{N-1} to $\frac{\pi}{2}$, and approaches infinity as $\theta \to \frac{\pi}{2}$. Because we can only use finite simulation data to fit $\rho_b^{*N}(\theta)$, there is some uncertainty in $\rho_b^{*N}(\theta)$, which further leads to the uncertainty of γ_N. However, we remark that there is no uncertainty in determination of $\rho_b^{*n}(\theta)$ and γ_n for $n < N$. Furthermore, as N increases, the value of γ_N decreases. Therefore, to compute η_L in the presence of attractive potentials, we iteratively increase N until the inequality $\frac{\gamma_N}{\sum_{n=1}^{n=N-1}\gamma_n} < 0.01$ is satisfied, and then approximate $\eta_{L,0} = 3(\sum_{n=1}^{n=N-1}\gamma_n)$. Because the assumed functional form for θ_n converges quickly to $\frac{\pi}{2}$ and because the assumed form for $\rho_b^{*n}(\theta)$ captures trajectory calculation results well, $N \leqslant 5$ is employed in most instances.

For low-St simulations, the assumption that collision occurs for all $\rho^*(\theta) \leqslant \rho_b^*(\theta)$ is found valid. However, at St = 5 and St = 10, the two largest Stokes numbers examined, "pockets" within the collision area are found. These are regions of initial positions for which $\rho^*(\theta) \leqslant \rho_b^*(\theta)$ and collision does not occur, but which are completely circumscribed by a region of initial positions for which collision does occur. Such cases require corrections to the enhancement factor; to determine the bounds of pockets we examined trajectories with particle i released from a structured square grid within the bounds of $\rho_b^*(\theta)$, with a grid spacing of 0.01 dimensionless units. From these calculations we extract $\rho_i^*(\theta)$ and $\rho_o^*(\theta)$, the inner and outer radii of the pocket at the angle θ, respectively, as well as θ_1 and θ_2, the minimum and maximum angles where the pocket exists. The enhancement factor is then calculated correcting for the pocket area:

$$\eta_L = \eta_{L,0} - 3\int_{\theta_1}^{\theta_2}\int_{\rho_i^*(\theta)}^{\rho_o^*(\theta)} \rho^{*2} \times \cos(\theta)d\rho^* d\theta \quad \text{(attractive potentials)}. \tag{16b}$$

For repulsive interactions, the collision area is bounded, and in converse to the collisionless pockets found for attractive potentials, collisions only occur for $\rho_i^*(\theta) \leqslant \rho^* \leqslant \rho_o^*(\theta)$. The integral in Eq. (12) can thus be evaluated directly by summing up values of $y^* dS^*$ in the region where collision occurs; this region can be determined by releasing particle i from a structured square grid (again with a grid spacing of 0.01 dimensionless units, and with particle i released on the grid nodes).

III. RESULTS AND DISCUSSION

A. Calculation validation and relative trajectories

As enhancement factor calculations require implementation of trajectory calculations and subsequent numerical integration, it is critical to validate the method by determining enhancement factors through alternative means. We compare simulation results to those calculated more directly considering infinite Stokes number (St $\to \infty$, which signifies the influence of drag is negligible) with both attractive and repulsive Coulomb potentials. Though this situation is highly unphysical, as in order for shear to have an influence on particle motion the drag force must be significant, neglecting drag enables determination of the collision area boundaries directly from the conservation of energy and angular momentum for the colliding particles. Derived in the Supplemental Material [48] following the approach of Vasil'ev and Reiss [49] but incorporating linear shear in lieu of thermal motion, the enhancement factor for St $\to \infty$ considering attractive Coulomb potentials can be calculated as

$$\eta_L|_{\mathrm{St}\to\infty} = 3\int_0^{\frac{\pi}{2}}\int_0^{\sqrt{\frac{1}{2}+\frac{1}{2}\sqrt{1+\frac{8Q}{\cos^2(\theta)\mathrm{St}}}}} \rho^{*2}\cos(\theta)d\rho^* d\theta \times (\text{attractive}). \tag{17a}$$

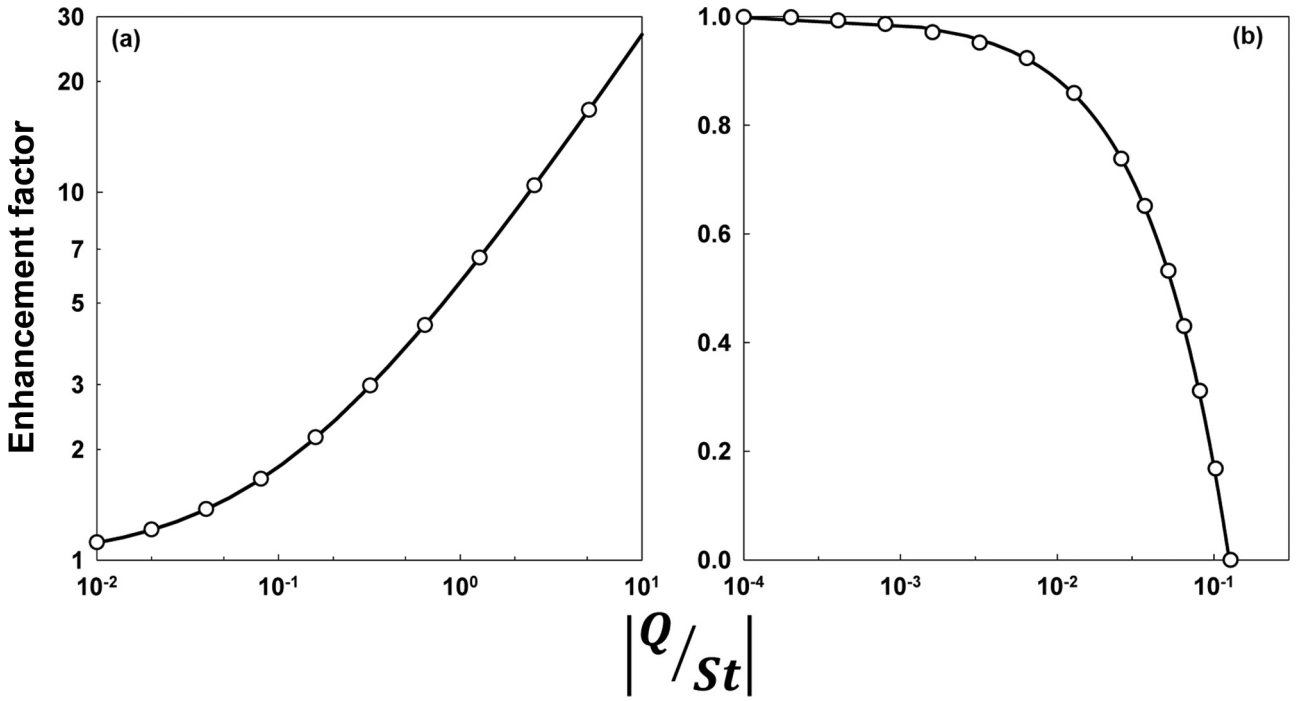

FIG. 2. The calculated enhancement factor in the presence of laminar or linear shear considering (a) attractive and (b) repulsive Coulomb interactions between particles in the St $\rightarrow \infty$ limit. Open symbols: trajectory calculation results. Lines: Eqs. (17a) and (17b) predictions.

For the repulsive Coulomb potential, the enhancement factor is expressed as

$$\eta_L|_{\mathrm{St}\rightarrow\infty} = 3\int_{\sqrt{\frac{1-\sqrt{1+8[Q/\mathrm{St}]}}{2}}}^{\sqrt{\frac{1+\sqrt{1+8[Q/\mathrm{St}]}}{2}}} \int_0^{\sqrt{1+\frac{2[Q/\mathrm{St}]}{y^{*2}}-y^{*2}}} y^* dx^* dy^* \quad \text{(repulsive)}. \tag{17b}$$

Equation (17b) applies for negative values of Q, and for sufficiently large Q it does not result in real numbers; in these instances $\eta_L|_{\mathrm{St}\rightarrow\infty} = 0$. The consequence of St $\rightarrow \infty$ is that in Eqs. (7a) and (7b) the drag term (rightmost term) can be neglected, with which it is evident that trajectory calculation results, similar to Eqs. (17a) and (17b), are dependent primarily on the parameter Q/St (which is the ratio of electrical energy to initial particle translational energy). Equations (17a) and (17b) calculations are plotted in comparison to trajectory calculation results in Figs. 2(a) and 2(b), respectively. Across multiple orders of magnitude in Q/St, we find excellent agreement with one another for both attractive and repulsive collisions; in most circumstances the two approaches agree to within 1% of one another, supporting the use of trajectory calculations for enhancement factor determination.

In total, we determined η_L for more than 400 distinct St, Q, and θ_r combinations, considering attractive and repulsive potentials, both with the Coulomb and conducting electrostatic potential functional forms. Tables S1–S4 in the Supplemental Material [48] summarize calculation results for St = 0, 0.5, 1.0, 5.0, and 10; each presented η_L is the result of more than 100 trajectory calculations, up to 2000 trajectories for instances where potential influences are large. In subsequent sections we discuss the results of these calculations considering attractive and repulsive interactions, respectively. However, first we examine selected relative trajectories of particles in the presence of attractive collisions in Fig. 3(a), considering complete electrostatic potential interactions. The boundary for collision, $(y_i^* - y_j^*)^2 + (z_i^* - z_j^*)^2 = 1$, is marked in the figure for each condition displayed. Particle motion at St = 0, the inertialess limit, is examined with simplified, first-order equations of motion; these equations can easily be derived from Eqs. (8a) and (8b). Elevated Stokes number relative trajectories result from direct implementation of Eqs. (8a) and (8b). At St = 0−1, the displayed trajectories reveal that at smaller initial separation distances (smaller $y_i^* - y_j^*$ in Fig. 3), collision occurs, while above a critical value, there is no collision. Additionally evident is that particles may "overshoot" one another (i.e., $z_i^* - z_j^*$ becomes negative prior to collision) and in many instances particle relative kinetic energy can approach zero at a relative location near $y_i^* - y_j^* = 0$, where there is little-to-no fluid driven differential motion. In such instances with attractive potentials, particles will be directed to collide with one another; this is evident first for one of the trajectories displayed at St = 1. At higher Stokes numbers (5 and 10), the overshoot and directed motion toward collision are even more pronounced, and in addition we find that particles can take orbitinglike trajectories, completing an entire revolution around one another. Experimentally, in the presence of differential settling (gravity) and electrostatic interactions, orbitinglike trajectories have been observed in the gas phase [5]; simulations here suggest that similar trajectories can be driven by shear and electrostatic forces. Interestingly, we also find at elevated Stokes number instances where collision does not occur in a narrow initial separation distance region, with the precise bounds of this region dependent on θ. This is evidenced in Fig. 3(b), which displays plots

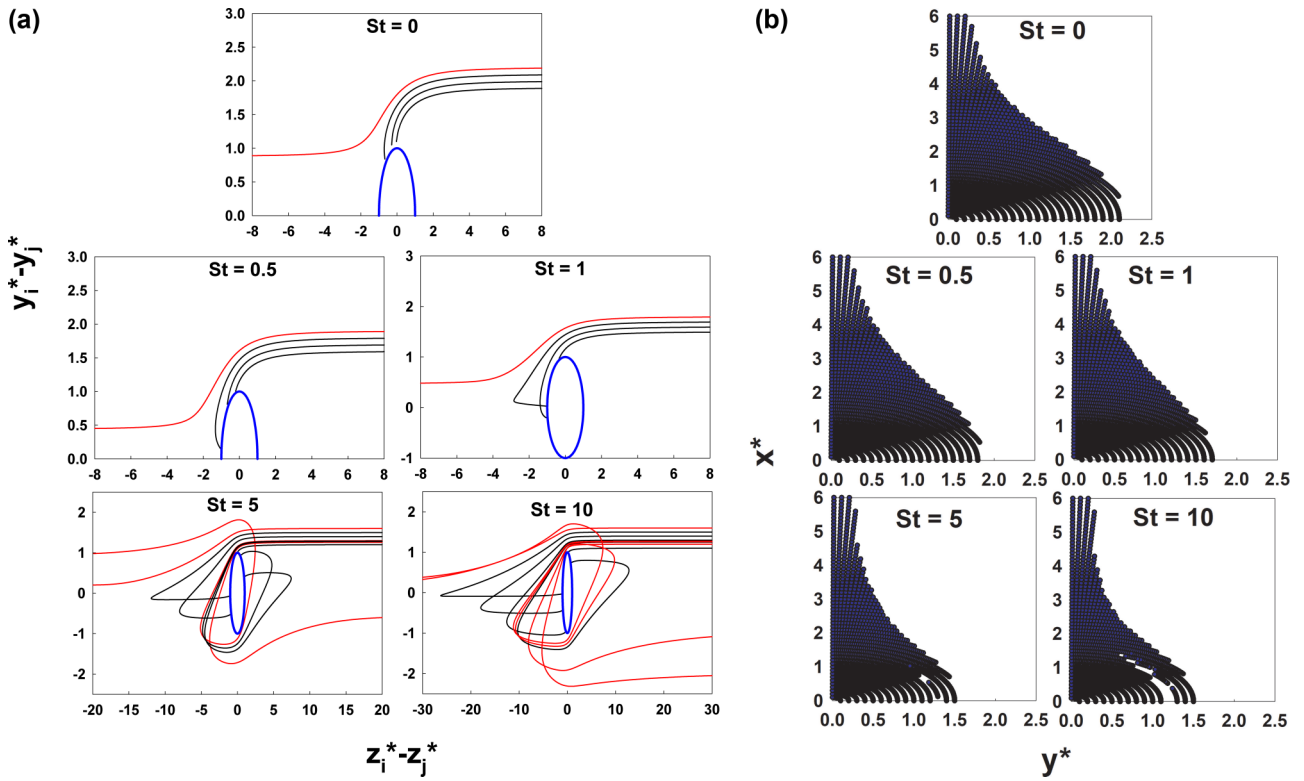

FIG. 3. (a) Selected relative particle trajectories (i.e., the motion of particle i from the perspective of particle j) for particles initiated on the y^*, z^* ($x^* = 0$) plane. Black lines denote collision, while red lines denote noncolliding trajectories. The blue line denotes the bound $(y_i^* - y_j^*)^2 + (z_i^* - z_j^*)^2 = 1$; hence it is the collision boundary. (b) Points corresponding to initial relative release points leading to collision. Collisionless pockets are evident at St = 5 and St = 10. For all instances, $Q = 1.56$ and $\theta_r = 1.0$, with the full electrostatic potential considered.

of all initial relative coordinates in trajectory calculations leading to collisions. The collisionless pockets are evident in Fig. 3(b) plots for St = 5 and St = 10. Such collisionless pockets, which necessitate the use of Eq. (16b) in enhancement factor calculations, only persist in instances where linear shear, inertia, and electrostatic interactions all have an influence on particle relative motion; they are not present for St = 0 (no inertia) conditions, St = ∞ (no shear gradient) conditions, and $Q = 0$ (no electrostatic interactions) conditions. Pockets are hence a unique feature of charged particle collision dynamics in gaseous media where particles can attain sufficiently high inertia.

B. Enhancement factor for attractive potentials

Though a simpler problem to examine, collisions in the inertialess limit (St = 0) are of interest for smaller particles; hence we examine this scenario first. Considering the Coulomb potential only and attractive potentials, the inertialess enhancement factor as $Q \to \infty$ can be analytically derived:

$$\eta_L|_{\mathrm{St}\to 0,\ Q\to\infty} = 3\pi Q. \tag{18}$$

Equation (18) leads to a dimensional collision rate coefficient which agrees exactly with the diffusion limited collision rate coefficient [24] at high potential energy to thermal energy ratios; this is because in both the laminar shear case and in the diffusive limit, only electrostatic forces and drag influence particle motion at high potential energy. In Fig. 4, we plot η_L as a function of Q considering both Coulomb and conducting electrostatic potentials at variable particle-size ratios (θ_r) for St = 0. Considering only the Coulomb

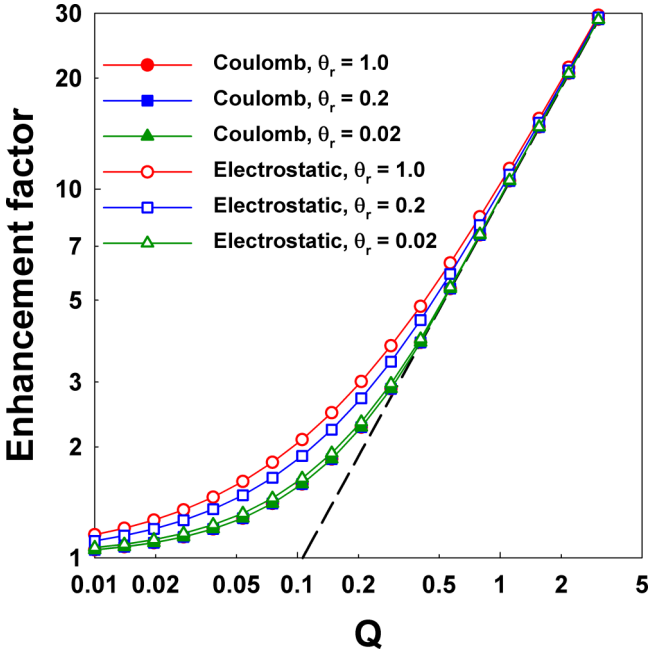

FIG. 4. The enhancement factor considering attractive potential interactions for St = 0. The black dashed line denotes Eq. (18) predictions.

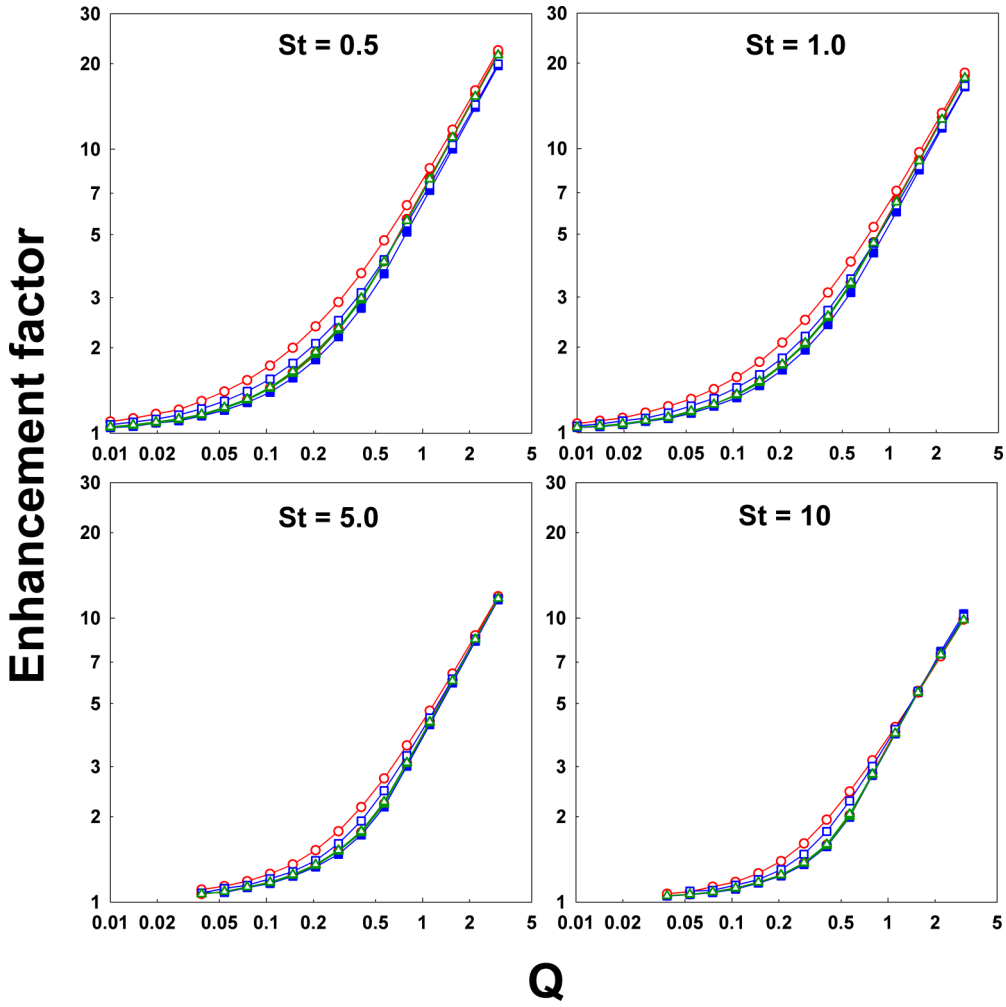

FIG. 5. The enhancement factor considering attractive potential interactions for St = 0.5−10. The legend provided in Fig. 4 applies to all displayed curves.

potential, the particle-size ratio is found to have a minimal influence on the enhancement factor; size influences are more pronounced for the complete electrostatic potential, with the largest enhancement factors observed for equal-sized particles with the electrostatic potential. Also noteworthy is that even for small values of Q (i.e., $Q = 0.1$) the enhancement factor takes on values greater than 1.5 for all examined conditions. In air at 300 K with a shear rate of $10\,\mathrm{s}^{-1}$, $Q = 0.1$ corresponds to a modest surface charge density of $44\,\mathrm{nC\,m}^{-2}$; hence calculations suggest that charged particle collisions in shear flows cannot be accurately modeled without considering the influence of the charge itself.

Plots analogous to Fig. 4 but for Stokes numbers in the 0.5–10 range are displayed in Fig. 5. Qualitatively, plots at elevated Stokes number are similar to the curves obtained for inertialess particles; $\eta_L \to 1$ as $Q \to 0$, the highest enhancement factors are obtained for equal-sized particles subjected to full electrostatic potentials, and at larger Q, η_L scales linearly with Q. However, enhancement factors for all Q are reduced at elevated Stokes numbers, e.g., for $Q = 0.21$, η_L decreases from 2.26 to 1.89 and then to 1.24 as St increases from 0 to 0.5 and then to 10, for equal-sized particles subject to the electrostatic potential. At larger Q, more pronounced St effects are evident, and η_L at $Q = 1.56$ evolves from 14.74 to 5.48 as St increases from 0 to 10. The decrease in η_L can be partially (but not entirely) attributed to the collision pockets formed at high Stokes number; for example, at $Q = 5.97$, St = 10, and $\theta_r = 0.2$, we find $\eta_{L,0} = 21.0$ while the pocket correction [Eq. (16b)] is 2.2 (leading to $\eta_L = 18.8$). These results collectively show that coupled with the influence of charge is the influence of particle inertia, and that neither can be neglected outright in modeling charged particle collisions in gaseous shear flows.

The influence of potentials on the enhancement factor is not well described by an additivity approximation, i.e., $\eta_L \neq 1 + 3\pi Q$. To parametrize results we fit results for equal-sized (and hence equal but opposite charge level) particles to the functional forms:

$$\eta_L = 1 + 3\pi Q b_3 \left[b_1 + (1 - b_1) \exp\left(-\frac{b_2}{Q} \right) \right]. \tag{19}$$

These functional forms match the large and small Q limiting functional forms by design. The values of b_1, b_2, and b_3 provided in Tables I and II for the Coulomb and complete electrostatic potentials, respectively, are found to

TABLE I. Equation (19) regression parameters for equal-sized particles considering the attractive Coulomb potential.

St	b_1	b_2	b_3
0	0.5104	0.2302	1.0000
0.01	0.5389	0.3103	1.0174
0.02	0.5364	0.2991	1.0074
0.05	0.5297	0.3070	0.9916
0.1	0.5321	0.3319	0.9638
0.2	0.5208	0.3170	0.8985
0.5	0.5253	0.3973	0.7672
1	0.5168	0.4734	0.6349
2	0.4689	0.5177	0.5141
5	0.2681	0.4106	0.4149
10	0.1584	0.4022	0.3805

TABLE II. Equation (19) regression parameters for equal-sized particles considering the attractive electrostatic potential.

St	b_1	b_2	b_3
0	0.9949	32.2759	1.0000
0.01	0.9790	5.0819	1.0160
0.02	0.9748	7.8983	1.0141
0.05	0.9909	2.5547	0.9743
0.1	0.8426	0.5888	0.9511
0.2	0.9671	2.0743	0.8931
0.5	0.9241	1.4361	0.763
1	0.8738	0.7967	0.6251
2	0.7882	0.5944	0.5072
5	0.6521	0.4555	0.3994
10	0.2601	0.0933	0.3132

match calculations extremely well (to within 1% of calculation results in most circumstances).

C. Enhancement factor for repulsive potentials

In all circumstances where long-range, repulsive interactions between particles are present, there will be a value of Q (absolute) above which the enhancement factor is zero. Therefore, an analogous expression to Eq. (18) need not be developed for repulsive potentials. Figure 6 displays plots of the enhancement factor versus $-Q$ for St = 0–10, considering both repulsive Coulombic and complete electrostatic potentials (with the latter a repulsive potential at large separation distances, and an attractive potential at close separation distances). For repulsive potentials, again the enhancement factor is higher for the complete electrostatic potential in comparison to the Coulomb potential, which is attributable to the close-range attraction incorporated into this potential form. While for purely attractive interactions particle inertia leads to decreased enhancement factors with increasing St, for repulsive potentials, the enhancement factor increases with increasing St, and drastically so. For example, at $Q =$

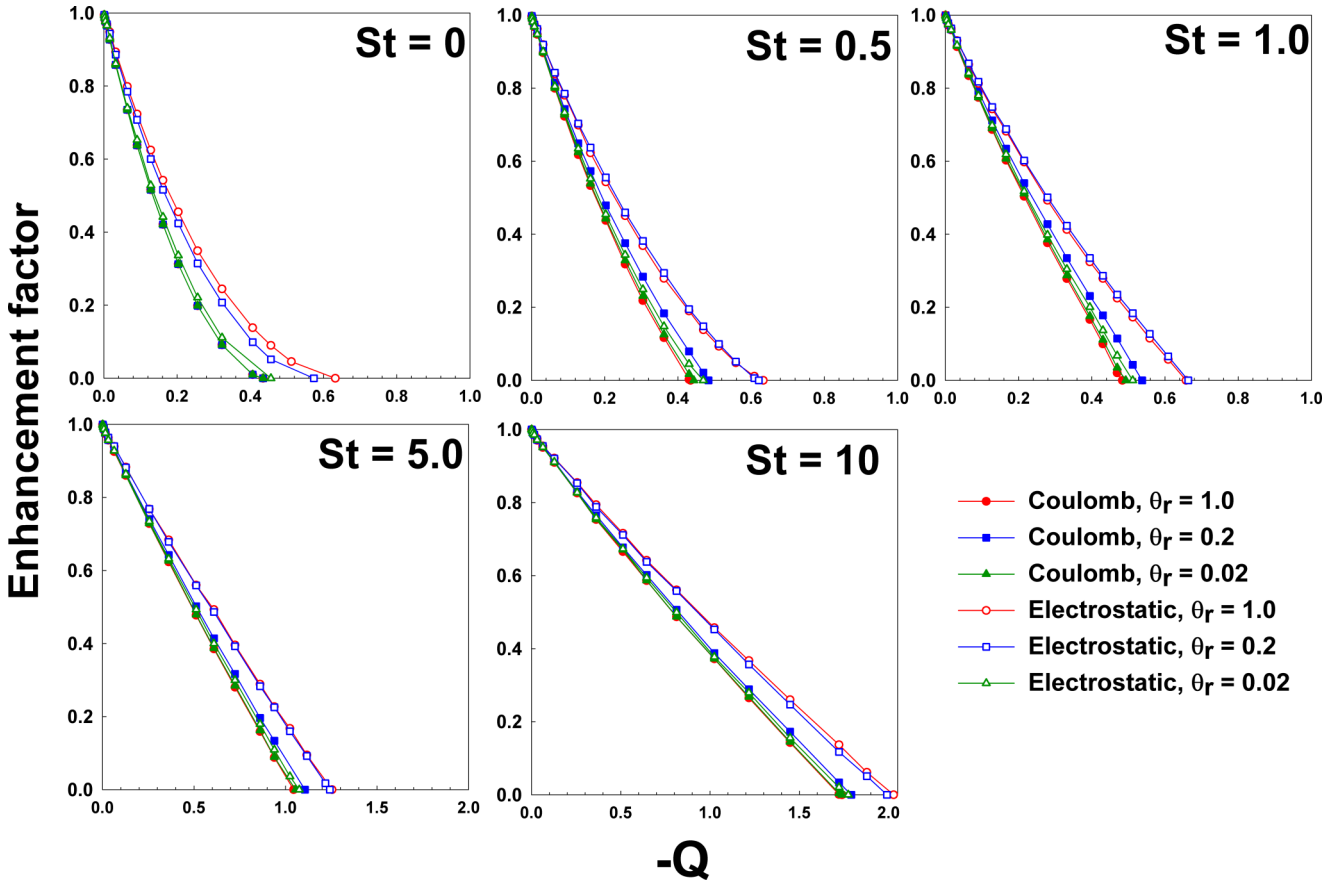

FIG. 6. The enhancement factor as a function of $-Q$ for repulsive interactions.

TABLE III. Equation (20) regression parameters for equal-sized particles subjected to the repulsive Coulomb potential.

St	c	Q_0
0	4.745	0.4348
0.01	4.689	0.4389
0.02	4.679	0.4348
0.05	4.498	0.4348
0.1	4.249	0.4308
0.2	3.689	0.4308
0.5	2.111	0.4348
1	0.888	0.4836
2	0.331	0.6211
5	0.123	1.0445
10	0.062	1.7392

-0.63, with St $= 0$, particle-particle collisions will not occur, irrespective of particle-size ratio. Under the same conditions but with St $= 10$, the enhancement factor remains above 0.55 (for all potentials and size ratios), suggesting that though repulsive interactions decrease the rate of particle-particle collisions, it remains similar in magnitude to that for uncharged particles.

For equal-sized particles, we fit repulsive potential results to the functional form:

$$\eta_L = cQ^2 + (cQ_0 + 1/Q_0)Q + 1, \quad |Q| < Q_0;$$
$$\eta_L = 0, \quad |Q| \geqslant Q_0. \tag{20}$$

Regression values for c and Q_0 (the absolute value of Q above which collisions no longer occur) are provided in Tables III and IV for the Coulomb and complete electrostatic potentials, respectively.

D. Comparison to diffusion limited collision rates

An interesting comparison is the collision rate for oppositely charged particles in the presence of a laminar shear gradient to that predicted by the diffusion limited reaction theory [31,36,50], i.e., evaluation of whether Brownian motion or differential fluid motion has a greater influence on charged particle collisions. Consideration of inertialess, equal-sized

TABLE IV. Equation (20) regression parameters for equal-sized particles subjected to the repulsive electrostatic potential.

St	c	Q_0
0	2.510	0.6322
0.01	2.471	0.6379
0.02	2.479	0.6321
0.05	2.431	0.6321
0.1	2.328	0.6321
0.2	2.130	0.6321
0.5	1.542	0.6332
1	0.759	0.6575
2	0.226	0.7820
5	0.078	1.2542
10	0.038	2.0282

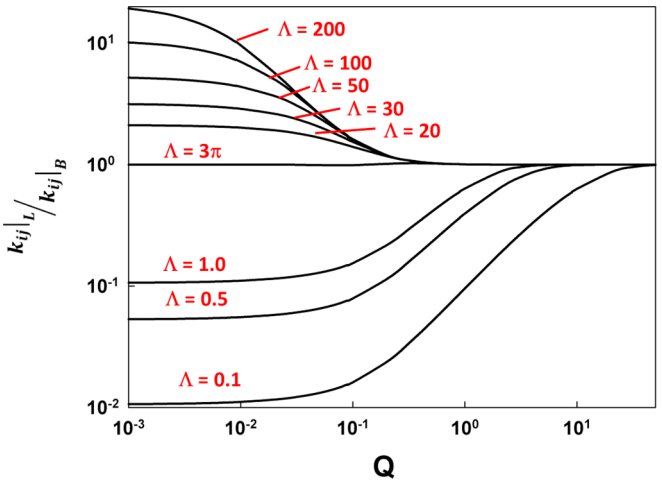

FIG. 7. The ratio of the laminar shear collision rate coefficient to the Brownian motion collision rate coefficient for oppositely charged particles, considering the Coulomb potential with St $= 0$.

particles and the Coulomb potential enables direct derivation of $\frac{k_{ij}|_L}{k_{ij}|_B}$, the laminar shear to Brownian motion collision rate coefficient:

$$\frac{k_{ij}|_L}{k_{ij}|_B} = [1 - \exp(-\Lambda Q)] \times \left\{ \frac{1}{3\pi Q} + \left[b_1 + (1 - b_1)\exp\left(\frac{-b_2}{Q} \right) \right] \right\}, \tag{21}$$

where $\Lambda = \frac{G f_{ij}(a_i + a_j)^2}{kT}$ is the shear energy to thermal energy ratio (kT is the thermal energy). Equation (21) is plotted in Fig. 7 for selected values of Λ. Immediately apparent is that only in instances of high Λ (larger than 3π) and modest values of Q (below 1) will the laminar shear collision rate exceed the Brownian motion collision rate. In converse to prior sections, which demonstrate the importance of considering both charge and inertial influences on particle-particle collisions in shear flows, Fig. 7 clearly shows that such phenomena need only be considered at high Λ. As Λ approximately scales with the cube of the particle radii (neglecting noncontinuum drag effects), shear based collisions hence become significant above a critical size, determined by $\Lambda = 3\pi$. In air at 300 K, with $G = 10\,\mathrm{s}^{-1}$, the critical particle radius is $1.78\,\mu$m, while at $G = 1\,\mathrm{s}^{-1}$, the critical radius increases to $3.85\,\mu$m. Though density dependent, particles in this size range would still have Stokes numbers close to 0 (St < 0.001 for unit density particles under both example conditions); with shear gradients in the $10^0 - 10^2\,\mathrm{s}^{-1}$ range Stokes number influences on collisions manifest themselves for particles with radii in excess of $10\,\mu$m.

IV. CONCLUSIONS

We have developed and utilized a trajectory based approach to determine the enhancement factor for collisions between charged particles in a laminar or linear field in a gas, accounting for finite particle inertia. Electrical effects are parametrized by the electrical energy to shear energy ratio (Q), while inertial effects are parametrized by the Stokes number (St). With the enhancement factor, particle-particle collision rates

can be calculated simply via Eq. (2b). We provide regression equations to better facilitate enhancement factor calculations for equal-sized particles charged to equal levels. Based on our computations, we make the following concluding remarks:

(1) In gaseous systems with appreciable shear gradients, the interplay between particle charge and particle inertia can strongly impact particle-particle collision rates. Use of simplified models of particle-particle collisions [i.e., Eq. (2a)] may lead to highly inaccurate predictions of collision rates, for both oppositely charged particles [where Eq. (2a) leads to underprediction] and particles of the same polarity (where it leads to overprediction). Particle inertia is found to lessen the influence of charge on collision, both for oppositely charged and like-charged particles, though not to the extent that charge effects can be ignored.

(2) At moderate to large Stokes numbers (i.e., 5–10), we find collisionless pockets in the collision area for attractive potentials, which are regions of relative initial particle positions where collision does not occur, but which are completely circumscribed by relative initial positions which lead to collision. Such pockets appear to be a unique result of inertia, shear, and electrostatic interactions all influencing particle motion.

(3) For charged particles (as well as uncharged particles, though not examined here), shear based motion need only be consider for modest Q levels and high shear energy to thermal energy ratios (above 3π). The shear energy to thermal energy ratio is strongly dependent on particle size, and is also influenced by gas viscosity, temperature, and through the friction coefficient, mean free path (if noncontinuum drag is considered). Above a critical size for any given system, shear induced motion is significantly more important than Brownian motion in driving particle-particle collisions. More refined analysis will be required to consider instances where shear induced motion, electrostatic interactions, inertia, and Brownian motion [51] all influence particle dynamics.

(4) The collision rate described in this work refers to the rate of initial collisions between two particles in a dilute system; whether particles bind and aggregate, rebound and exchange charge, or recollide [5] has not been considered here. To investigate these phenomena in future work the approach employed here will need to be coupled with models of adhesion (i.e., more detailed short-range potential interactions than the models employed here), charge exchange upon collision, and exchange of momentum and energy upon collision. Also not examined were aspherical particles and aggregates [23,52–54]; this will require consideration of alignment and rotation in flow, as well as an appropriate drag coefficient [55]. Finally, in many instances the dilute approximation is not valid, and multibody particle interactions (particularly electrostatic) will need to be considered in future collision modeling efforts.

ACKNOWLEDGMENTS

H.Y. acknowledges support from the 3M Fellowship. Partial support was also provided by the United States Army Research Office Award No. MURI W911NF-12-1-0407.

[1] N. I. Lebovka, in *Polyelectrolyte Complexes in the Dispersed and Solid State I: Principles and Theory*, edited by M. Muller (Springer-Verlag, Berlin, 2014), p. 57.
[2] A. A. Onischuk, S. di Stasio, V. V. Karasev, A. M. Baklanov, G. A. Makhov, A. L. Vlasenko, A. R. Sadykova, A. V. Shipovalov, and V. N. Panfilov, J. Aerosol. Sci. **34**, 383 (2003).
[3] S. Vemury and S. E. Pratsinis, J. Aerosol. Sci. **27**, 951 (1996).
[4] K. M. Forward, D. J. Lacks, and R. M. Sankaran, Phys. Rev. Lett. **102**, 028001 (2009).
[5] V. Lee, S. R. Waitukaitis, M. Z. Miskin, and H. M. Jaeger, Nat. Phys. **11**, 733 (2015).
[6] P. Mehrani, M. Murtomaa, and D. J. Lacks, J. Electrost. **87**, 64 (2017).
[7] O. Ishihara, J. Phys. D: Appl. Phys. **40**, R121 (2007).
[8] G. E. Morfill and A. V. Ivlev, Rev. Mod. Phys. **81**, 1353 (2009).
[9] L. C. J. Heijmans and S. Nijdam, EPL **114**, 64004 (2016).
[10] D. J. Lacks and R. M. Sankaran, J. Phys. D: Appl. Phys. **44**, 453001 (2011).
[11] T. Pahtz, H. J. Herrmann, and T. Shinbrot, Nat. Phys. **6**, 364 (2010).
[12] R. Yoshimatsu, N. A. M. Araújo, G. Wurm, H. J. Herrmann, and T. Shinbrot, Sci. Rep. **7**, 39996 (2017).
[13] T. Shinbrot and H. J. Herrmann, Nature **451**, 773 (2008).
[14] M. F. Al-Adel, D. A. Saville, and S. Sundaresan, Ind. Eng. Chem. Res. **41**, 6224 (2002).
[15] D. J. Lacks and R. M. Sankaran, Part. Sci. Technol. **34**, 55 (2016).
[16] U. Kortshagen and U. Bhandarkar, Phys. Rev. E **60**, 887 (1999).
[17] R. Le Picard, A. H. Markosyan, D. H. Porter, S. L. Girshick, and M. J. Kushner, Plasma Chem. Plasma Process. **36**, 941 (2016).
[18] L. Ravi and S. L. Girshick, Phys. Rev. E **79**, 026408 (2009).
[19] T. Matsoukas and M. Russell, J. Appl. Phys. **77**, 4285 (1995).
[20] T. Matsoukas, M. Russell, and M. Smith, J. Vac. Sci. Technol., A **14**, 624 (1996).
[21] W. H. Marlow, J. Chem. Phys. **73**, 6284 (1980).
[22] D. D. Huang, J. H. Seinfeld, and K. Okuyama, J. Colloid Interface Sci. **141**, 191 (1991).
[23] A. Shahravan, C. Lucas, and T. Matsoukas, J. Appl. Phys. **108**, 083303 (2010).
[24] N. A. Fuchs, *The Mechanics of Aerosols*, revised and enlarged ed. (Macmillan, New York, 1964).
[25] R. Hogg, T. W. Healy, and D. W. Fuerstenau, Trans. Faraday Soc. **62**, 1638 (1966).
[26] H. M. Mott-Smith and I. Langmuir, Phys. Rev. **28**, 727 (1926).
[27] J. E. Allen, Phys. Scr. **45**, 497 (1992).
[28] J. Goree, Plasma Sources Sci. Technol. **3**, 400 (1994).
[29] N. A. Fuchs, Geofis. Pura Appl. **56**, 185 (1963).
[30] W. A. Hoppel and G. M. Frick, Aerosol Sci. Technol. **5**, 1 (1986).
[31] R. Gopalakrishnan and C. J. Hogan, Phys. Rev. E **85**, 026410 (2012).
[32] R. Gopalakrishnan, T. Thajudeen, H. Ouyang, and C. J. Hogan, J. Aerosol. Sci. **64**, 60 (2013).
[33] A. A. Lushnikov and M. Kulmala, Phys. Rev. E **70**, 046413 (2004).
[34] J. Porstendorfer, G. Robig, and A. Ahmed, J. Aerosol. Sci. **10**, 21 (1979).

[35] M. Adachi, Y. Kousaka, and K. Okuyama, J. Aerosol. Sci. **16**, 109 (1985).
[36] T. Matsoukas, J. Colloid Interface Sci. **187**, 474 (1997).
[37] L. G. B. Bremer, P. Walstra, and T. Vanvliet, Colloids Surf., A **99**, 121 (1995).
[38] M. Von Smoluchowski, Z. Phys. **17**, 557 (1916).
[39] M. Vanni and G. Baldi, Adv. Colloid Interface Sci. **97**, 151 (2002).
[40] D. N. Thomas, S. J. Judd, and N. Fawcett, Water Res. **33**, 1579 (1999).
[41] K. Higashitani, R. Ogawa, G. Hosokawa, and Y. Matsuno, J. Chem. Eng. Jpn. **15**, 299 (1982).
[42] M. D. Allen and O. G. Raabe, Aerosol Sci. Technol. **4**, 269 (1985).
[43] L. A. Spielman, J. Colloid Interface Sci. **33**, 562 (1970).
[44] P. Saffman, J. Fluid Mech. **22**, 385 (1965).
[45] J. Lekner, Proc. R. Soc. A **468**, 2829 (2012).
[46] J. H. Jeans, *The Mathematical Theory of Electricity and Magnetism* (University Press, Cambridge, UK, 1908).
[47] T. Thajudeen, R. Gopalakrishnan, and C. J. Hogan, Aerosol Sci. Technol. **46**, 1174 (2012).
[48] See Supplemental Material at http://link.aps.org/supplemental/10.1103/PhysRevE.96.032911 for Tables S1–S4, summarizing calculation results, and Fig. S1 and Table S5, showing an example regression result used in collision area boundary determination. Derivation of Eqs. (17a) and (17b) are also available online.
[49] O. V. Vasil'ev and H. Reiss, J. Chem. Phys. **105**, 2946 (1996).
[50] L. G. D'yachkov, A. G. Khrapak, S. A. Khrapak, and G. E. Morfill, Phys. Plasmas **14**, 042102 (2007).
[51] Y. Drossinos and M. W. Reeks, Phys. Rev. E **71**, 031113 (2005).
[52] W. R. Heinson, C. M. Sorensen, and A. Chakrabarti, Langmuir **28**, 11337 (2012).
[53] C. M. Sorensen and A. Chakrabarti, Soft Matter **7**, 2284 (2011).
[54] L. Isella and Y. Drossinos, Phys. Rev. E **82**, 011404 (2010).
[55] C. Zhang, T. Thajudeen, C. Larriba, T. E. Schwartzentruber, and C. J. Hogan, Aerosol Sci. Technol. **46**, 1065 (2012).